Chapter 1

INTRODUCTION

1.1. RESONANCES IN SCATTERING THEORY

Scattering resonances are the replacement of discrete spectral data for problems on non-compact domains. The possibility of escape to infinity means that in addition to initial energy (the eigenvalue in the compact setting) we also have a rate of decay. It turns out that this information can be encoded as a pole of the *meromorphic continuation* of the resolvent/Green function.

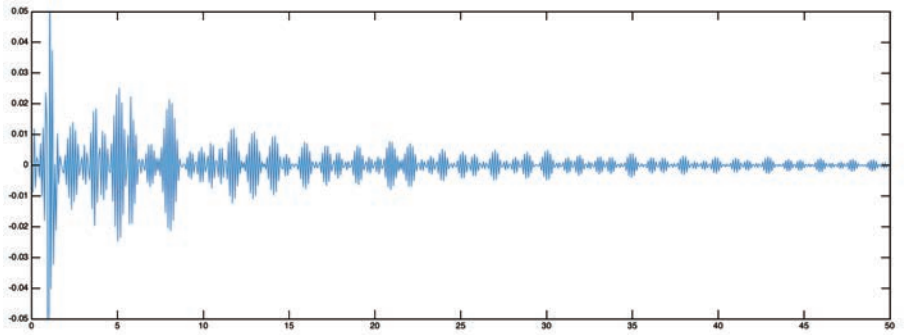

Figure 1.1. The plot of $u(t, 0)$ showing oscillations and decay of the solution in the interaction region. The full $u(t, x)$ is shown in Figure 1.2.

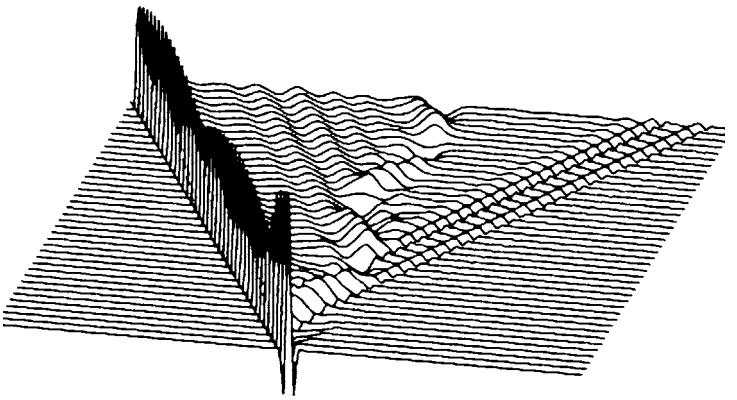

Figure 1.2. A solution of the wave equation $\partial_t^2 u - \partial_x^2 u + V(x)u = 0$ where V is shown in Figure 1.3. The initial data is localized near 0. The time axis points away from the viewer.

The simplest setting in which this can be seen is given by the operator $P = -\partial_x^2$ on the real line, $\mathbb{R}$. The resolvent $R_0(\lambda) := (P - \lambda^2)^{-1} : L^2(\mathbb{R}) \to L^2(\mathbb{R})$ is a bounded operator for $\lambda \notin \mathbb{R}$. It is given explicitly as follows:

$$R_0(\lambda) f(x) = \int_{\mathbb{R}} R_0(\lambda, x, y) f(y)\, dy,$$
$$R_0(\lambda, x, y) = \frac{i}{2\lambda} e^{i\lambda|x-y|}, \quad \operatorname{Im} \lambda > 0.$$

For fixed x and y, $R_0(\lambda, x, y)$ continues to a meromorphic function of λ with one pole at $\lambda = 0$. This pole is the *scattering resonance* of P. Its dynamical significance is most easily seen in the context of the wave equation

$$(\partial_t^2 - \partial_x^2) u(t, x) = 0, \quad u(0, x) = 0, \quad \partial_t u(0, x) = f(x),$$
$$u(t, x) = \frac{1}{2} \int_{x-t}^{x+t} f(y)\, dy.$$

If $f(x) = 0$ for $|x| > R$, then

$$u(t, x) = \frac{1}{2} \int_{\mathbb{R}} f(y)\, dy \quad \text{for } t > |x| + R.$$

In terms of $R_0(\lambda, x, y)$ this can be reinterpreted as follows:

$$u(t, x) = -i \int_{\mathbb{R}} (\operatorname{Res}_{\lambda=0} R_0(\lambda, x, y))\, f(y)\, dy, \quad \operatorname{Res}_{\lambda=0} R_0(\lambda, x, y) = \frac{i}{2}.$$

This means that the residue of R_0 at the pole describes *long-time behavior* (in t) of the wave in compact sets (in x).

A more interesting mathematical example – studied in detail in Chapter 2 – involves scattering by a compactly supported potential, V, in dimension one; see Figure 1.3 for an example. Scattering resonances are the rates

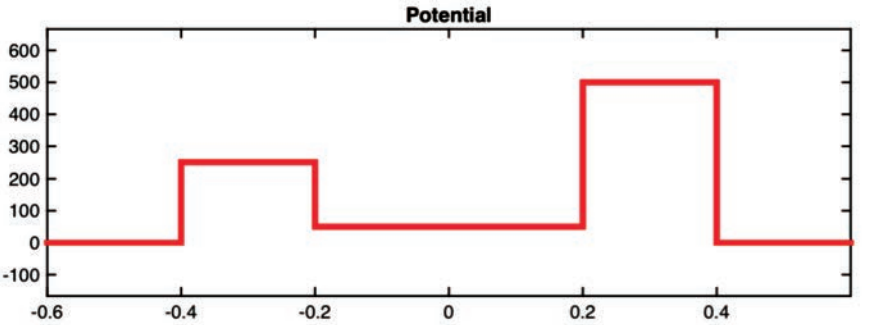

Figure 1.3. A simple one-dimensional potential used to see trapping and tunneling of the wave in Figures 1.1 and 1.2.

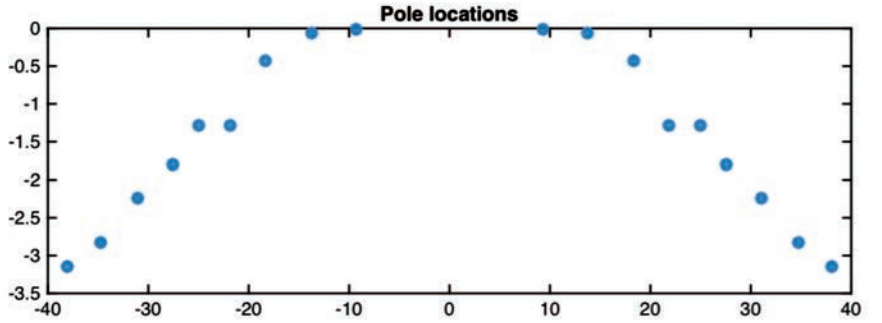

Figure 1.4. Scattering resonances of the potential shown in Figure 1.3. They are computed using the code `squarepot.m` by David Bindel [**BZ**].

of oscillation and decay of solutions of the wave equation

$$(\partial_t^2 - \partial_x^2 + V(x))u = 0 \tag{1.1.1}$$

with localized initial data. Figures 1.1 and 1.2 show such a solution: we see the main wave escape and some trapped waves bounce in the well created by the potential and leak out. Instead of the eigenfunction expansion (which would hold if x took values in the circle $\mathbb{R}/\mathbb{Z}$) we have the *resonance expansion*

$$u(t,x) = \sum_{\operatorname{Im}\lambda_j > -A} e^{-i\lambda_j t} u_j(x) + \mathcal{O}_K(e^{-tA}), \quad x \in K \Subset \mathbb{R}.$$

Here the *scattering resonances* λ_j are complex numbers with $\operatorname{Im}\lambda_j \leq 0$ which are independent of the initial data – see Theorem 2.9 for the precise statement. We clearly see that

$$\begin{aligned} \operatorname{Re}\lambda_j &= \text{rate of oscillation,} \\ -\operatorname{Im}\lambda_j &= \text{rate of decay.} \end{aligned}$$

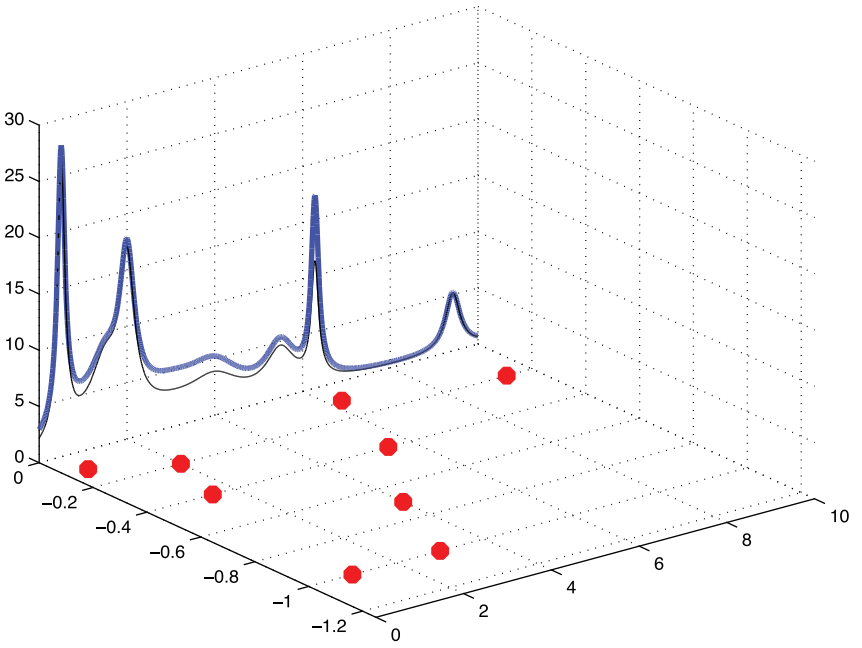

Figure 1.5. The power spectrum on the real line (Fourier transform) of correlations $\rho_{f,g}(t) = \langle U(t)f, g\rangle$: the blue and black plots show $\lambda \mapsto |\int_0^\infty \rho_{f,g}(t)e^{-i\lambda t}dt|$ for two different choices of f and g. Here $U(t)$ could be the propagator of the wave equation (1.1.1), or it could be for instance the pullback by an Anosov flow – see [**Zw17**, Chapter 4]. Resonances are the poles of the meromorphic continuation of the power spectrum to the complex plane, and this figure shows a schematic correspondence between resonances and the power spectrum: $\operatorname{Re}\lambda_j$ corresponds to the location of a peak in the power spectrum and $\operatorname{Im}\lambda_j$ to its width.

The terms $u_j(x)$ are calculated using the residues of the meromorphic continuation of $R_V(\lambda) = (P - \lambda^2)^{-1}$, $P := -\partial_x^2 + V(x)$, just as we saw above in the case of $V \equiv 0$. To explain why meromorphic continuation appears we use the *power spectrum*, which is the Fourier transform of u in time:

$$\widehat{u}(\lambda, x) := \int_0^\infty e^{i\lambda t} u(t, x)\, dt, \quad \operatorname{Im}\lambda > 0.$$

The resonance expansion implies that for all A,

$$\widehat{u}(\lambda, x) - i \sum_{\operatorname{Im}\lambda_j > -A} \frac{u_j(x)}{\lambda - \lambda_j} \quad \text{extends holomorphically to } \{\operatorname{Im}\lambda > -A\}.$$

Thus $\widehat{u}(\lambda, x)$ extends meromorphically to $\lambda \in \mathbb{C}$, with poles at λ_j. Writing $\widehat{u}(\lambda, x)$ in terms of f and the scattering resolvent $R_V(\lambda)$, we obtain the

definition of resonances used in this book:

$$\text{resonances} \;=\; \text{poles of the scattering resolvent.}$$

Harmonic inversion methods, the first being the celebrated Prony algorithm [**Pr95**], can then be used to extract scattering resonances (see for instance [**WMS88**]) from the power spectrum $\widehat{u}(\lambda, x)$ for λ real. See Figures 1.4 and 1.5.

Although this book is intended for a mathematical audience and concentrates on rigorous presentation, physical motivation plays an essential role in the study of scattering resonances. Even when, as for instance in scattering on the modular surface, the questions have purely mathematical context, the origins lie in physics and it is easiest to relate them in the setting of quantum mechanics.

In quantum mechanics a particle is described by a wave function ψ which is normalized in L^2, $\|\psi\|_{L^2} = 1$. The probability of finding the particle in a region Ω is given by the integral of $|\psi(x)|^2$ over Ω. If $\psi = \psi_k$ is an eigenstate of a quantum Hamiltonian P (here k is a quantum number or the index of the discrete spectrum), the time-evolved state is given by

$$\psi_k(t) := e^{-itP}\psi_k = e^{-itE_k}\psi_k \quad \text{where} \quad P\psi_k = E_k\psi_k. \tag{1.1.2}$$

In particular the probability density does not change when the state is propagated.

An example could be given by the Bloch electron in a quantum corral as shown in Figures 1.6 and 1.9. The graphs in these figures depict the derivative of the density of states as a function of the voltage (which for us is the energy E), which measures the response of the quantum system when excited at energy E.

However, the same figures also show that the measured states have nonzero "widths" – the peak is not a delta function at E_k – and hence can be more accurately modeled by resonances. The following standard argument from the physics literature explains the meaning of the real and imaginary parts: the time evolution of a pure resonant state corresponding to a resonance $\lambda_k^2 = E_k - i\Gamma_k/2$ is given by the following modification of (1.1.2):

$$\psi_k(t) = e^{-itE_k - t\Gamma_k/2}\psi_k.$$

Thus the probability of survival beyond time t is $p(t) = |\psi_k(t)|^2/|\psi_k(0)|^2 = e^{-\Gamma_k t}$. This explains why the convention for the imaginary part of a resonance is $\Gamma_k/2$. Here we neglected the issue that $\psi_k \notin L^2$, which is remedied by taking the probabilities over a bounded interaction region. In the energy

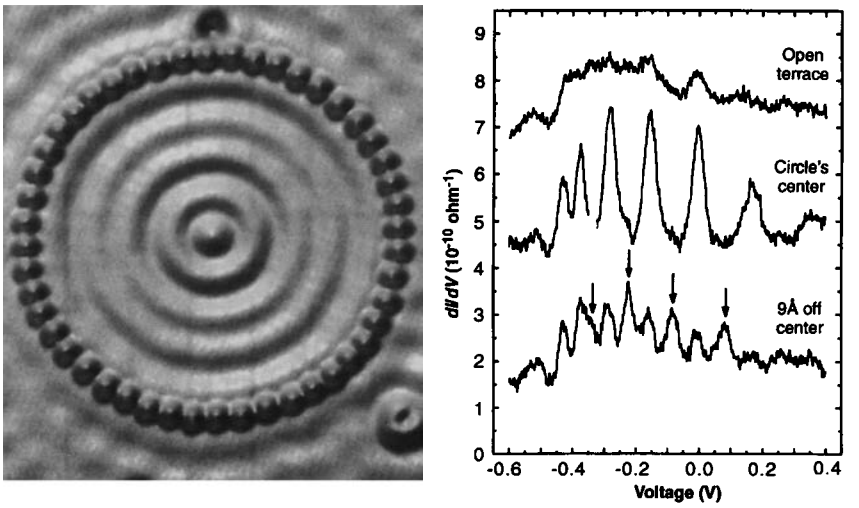

Figure 1.6. Experimental set-up and data in a scanning tunneling microscope experiment by Crommie et al. [**CLE93**] from IBM's Almaden Research Center. The figure on the left shows a quantum corral formed by 48 iron atoms on a copper Cu(111) surface. The plot on the right shows measurements of dI/dV (I being the current) as functions of voltage V from different positions of the microscope tip: outside the corral (open terrace) at the center, and off-center. The peaks show resonances – see Figure 1.5 for a schematic representation and Figure 2.6 for a simple mathematical example. The new states visible with an off-center measurement are shown with arrows.

representation the wave function is given by the Fourier transform in time,

$$\begin{aligned}\varphi_k(E) &:= \frac{1}{\sqrt{2\pi}} \int_0^\infty e^{itE} \psi_k(t)\, dt \\ &= \frac{1}{\sqrt{2\pi} i} \frac{\psi_k}{E_k - i\Gamma_k/2 - E},\end{aligned}$$

which means that the probability density of the time evolved resonant state $\psi_k(t)$ at energy E is proportional to the square of the absolute value of the right hand side. Consequently, this probability density is

$$\frac{1}{2\pi} \frac{\Gamma_k}{(E - E_k)^2 + (\Gamma_k/2)^2}\, dE, \tag{1.1.3}$$

and this Lorentzian is the famous *Breit–Wigner distribution*. To see how this vague discussion works out mathematically, see Theorem 2.20 and the references in §§3.13 and 7.6.

In practice there are many deviations from the simple formula (1.1.3), especially at high energies and in the presence of overlapping resonances. In Figures 1.6 and 1.9 we see that clear Lorentzian peaks and individual

resonances can be recovered. In the experiment whose set-up is shown in Figure 1.11, the resonances overlap and the peaks in the scattering data do not have the simple interpretation using (1.1.3). Figure 2.6 illustrates a mathematical result related to the Breit–Wigner approximation.

For bound states the *Weyl law* (see [**Iv16**] for history and references) provides an asymptotic formula for the density of states. Weyl laws for counting resonant states are more complicated and richer as they involve both energy and rates of decay. Even the leading term can be affected by dynamical properties of the system.

1.2. SEMICLASSICAL STUDY OF RESONANCES

For some very special systems resonances can be computed explicitly. One famous example is the Eckart barrier: $-\partial_x^2 + \cosh^{-2} x$. It falls into the general class of Pöschl–Teller potentials, which can also be used to compute resonances of the Laplace–Beltrami operator for hyperbolic spaces or hyperbolic cylinders – see for instance [**GZ95a**] or [**Bo16**]. Another example is given by the sphere, in which case scattering resonances are zeros of Hankel functions which can be described asymptotically – see [**St06**] and Figure 1.7.

In general, however, it is impossible to obtain an explicit description of individual resonances. Hence we need to consider their properties and their distribution in asymptotic regimes. For example in the case of obstacle

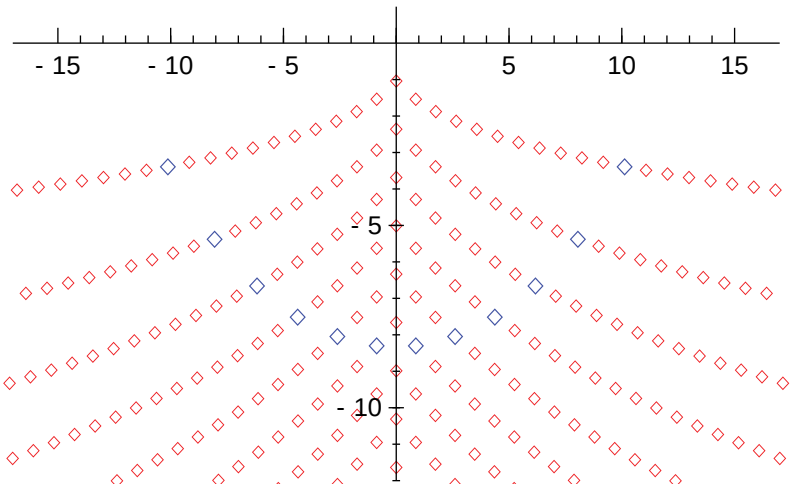

Figure 1.7. Resonances for the sphere (of radius one) in three dimensions. For each spherical momentum ℓ they are given by solutions of $H^{(2)}_{\ell+1/2}(\lambda) = 0$ where $H^{(2)}_\nu$ is the Hankel function of order ν. Each zero appears as a resonance of multiplicity $2\ell+1$; the resonances with $\ell = 12$ are highlighted.

scattering that could mean the high-energy limit. In the case of the sphere in Figure 1.7 that corresponds to letting the angular momentum $\ell \to +\infty$. For a general obstacle that means considering resonances as $|\lambda| \to +\infty$ and $|\operatorname{Im}\lambda| \ll |\lambda|$.

The high-energy limit is a special case of the *semiclassical* limit. For instance, we can consider resonances of the Dirichlet realization of $-h^2\Delta + V$ on $\mathbb{R}^n \backslash \mathcal{O}$ in bounded subsets of $\mathbb{C}$ as $h \to 0$. When $V \equiv 0$ that corresponds to the high-energy limit for obstacle problems, and when $\mathcal{O} = \emptyset$ it corresponds to Schrödinger operators.

In the case of semiclassical Schrödinger operators, the properties of the classical energy surface $\xi^2 + V(x) = E$ can be used to study resonances close to $E \in \mathbb{R}$. Some aspects of that will be presented in §2.8 in one dimension and in Chapters 6 and 7 in more depth. Figure 1.8 shows some of the principles in dimension one. The last set of resonances shown there and labeled as Regge resonances comes from the singularities at the boundary of the support of the potential V shown there. Roughly speaking, these resonances are responsible for large-energy asymptotics for the number of resonances given in Theorem 2.16.

1.3. SOME EXAMPLES

We present here a few examples of scattering resonances appearing in physical systems.

A textbook example of scattering resonances is related to tunneling through potential barriers. Resonances generated by that process are the *shape resonances* shown in Figure 1.8. Figure 7.1 illustrates a similar potential (plotted against the "reaction coordinate") motivated by an actual energy landscape of a chemical reaction. Only recently have experiments caught up with this well-known theory, as shown by the following quote from a survey lecture [**Cl18**]: "Quantum scattering resonances in chemical reactions have long been of interest to theoreticians but have only relatively recently been experimentally measured." We refer to [**Cl18**] for many interesting examples of different reactions with varied energy landscapes (e.g. $\mathrm{F} + \mathrm{H_2} \to \mathrm{HF} + \mathrm{H}$,[1] $\mathrm{F} + \mathrm{CHD_3} \to \mathrm{FH} + \mathrm{CD_3}$, and $\mathrm{O} + \mathrm{O_2} \to \mathrm{O_3}$, the last being a very important process in the Earth's atmosphere).

[1] It is irresistible to recall the following small anecdote: One of the authors returned from a discussion with William H. Miller of the Chemistry department, a major contributor to the subject, to the Mathematics department, and his very pure mathematical French visitor mockingly asked, "What reactions were you discussing?" The answer was the reaction above. Our colleague's response was, "I am relieved – I was worried you were doing something useful."

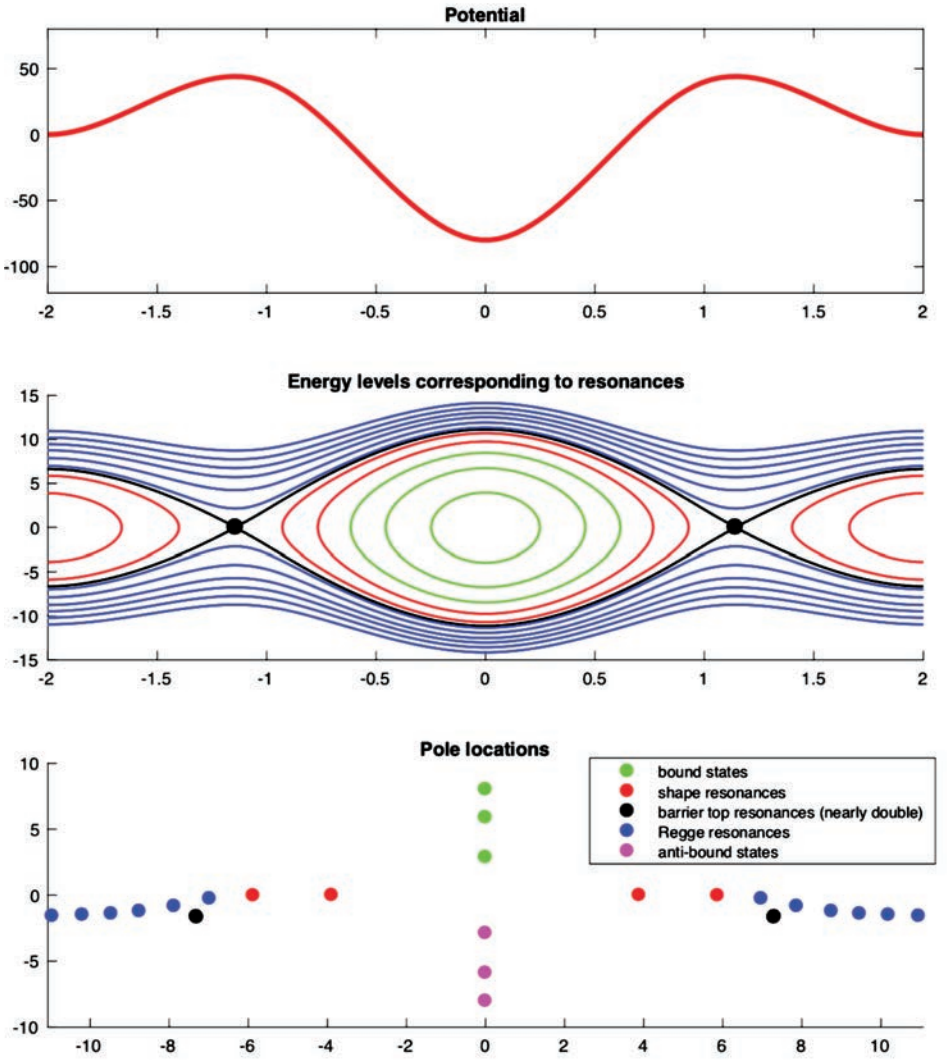

Figure 1.8. Resonances corresponding to different dynamical phenomena. The bound states are generated by negative level sets of $\xi^2+V(x)$ satisfying Bohr–Sommerfeld quantization conditions. Bounded positive level sets of $\xi^2 + V(x)$ can also satisfy the quantization conditions, but they cannot produce bound states – tunneling to the unbounded components of these level sets is responsible for resonances with exponentially small ($\sim e^{-S/h}$) imaginary parts/width – see §§2.8 and 7.3 and references in the notes to the corresponding chapters. The unstable trapped points corresponding to maxima of the potential produce resonances which are at distance h from the real axis – see §§6.3 and 6.6. The Regge resonances with $\operatorname{Im}\lambda \sim -\log \operatorname{Re}\lambda$ come from the singularities at the boundary of the support of the potential – see [**Re58**] and [**Zw87**]. The anti-bounds are defined here as resonances on the negative imaginary axis – see [**Si00**] and [**DG10**]. The resonances are computed using the code `splinepot.m` by David Bindel [**BZ**].

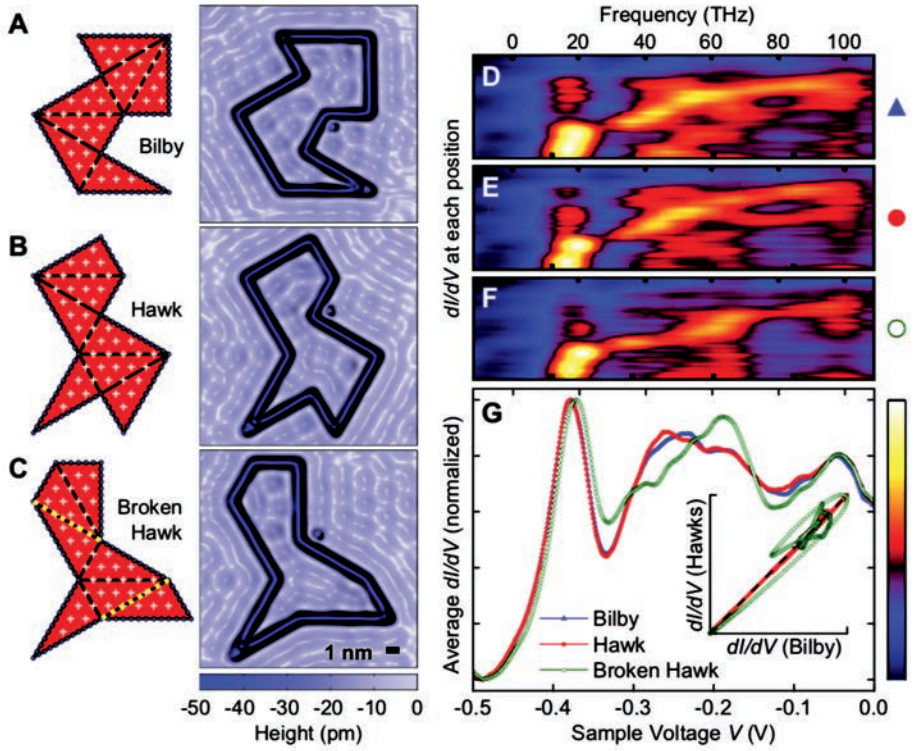

Figure 1.9. A scanning tunneling microscope (STM) experiment from the Manoharan lab at Stanford University [**M*****08**]. The figure shows design and realization of quantum isospectral resonators each assembled from 90 CO molecules on the Cu(111) surface. An STM spectrum is a plot of dI/dV(I being the current) as a function of the bias voltage V. Each spectrum shows the series of surface state electron resonances inside a bounded quantum corral – see Figure 1.5 for a visualization of the relation between the peaks and the complex resonances. (A to C) Schematics and STM topographies of the Bilby (A), Hawk (B), and Broken Hawk (C) domains. The seven identical $\pi/6$-$\pi/3$-$\pi/2$ triangles composing each shape are shown in red. Blue dots indicate the positions of wall molecules. White crosses mark locations where dI/dV spectroscopy was performed. STM topographs are 15 nm by 15 nm (V = 10 mV, I = 1 nA). A single CO molecule used for registration between spectra accompanies each nanostructure. (D to F) Spectral fingerprints (dI/dV spectra) acquired throughout Bilby (D), Hawk (E), and Broken Hawk (F). (G) The normalized averages of the Bilby and Hawk spectra match closely, consistent with isospectrality, whereas the average Broken Hawk spectrum clearly differs. Inset: Spectral correlation plot (dashed line indicates perfect match) quantifying Bilby–Hawk isospectrality and its departure in Broken Hawk.

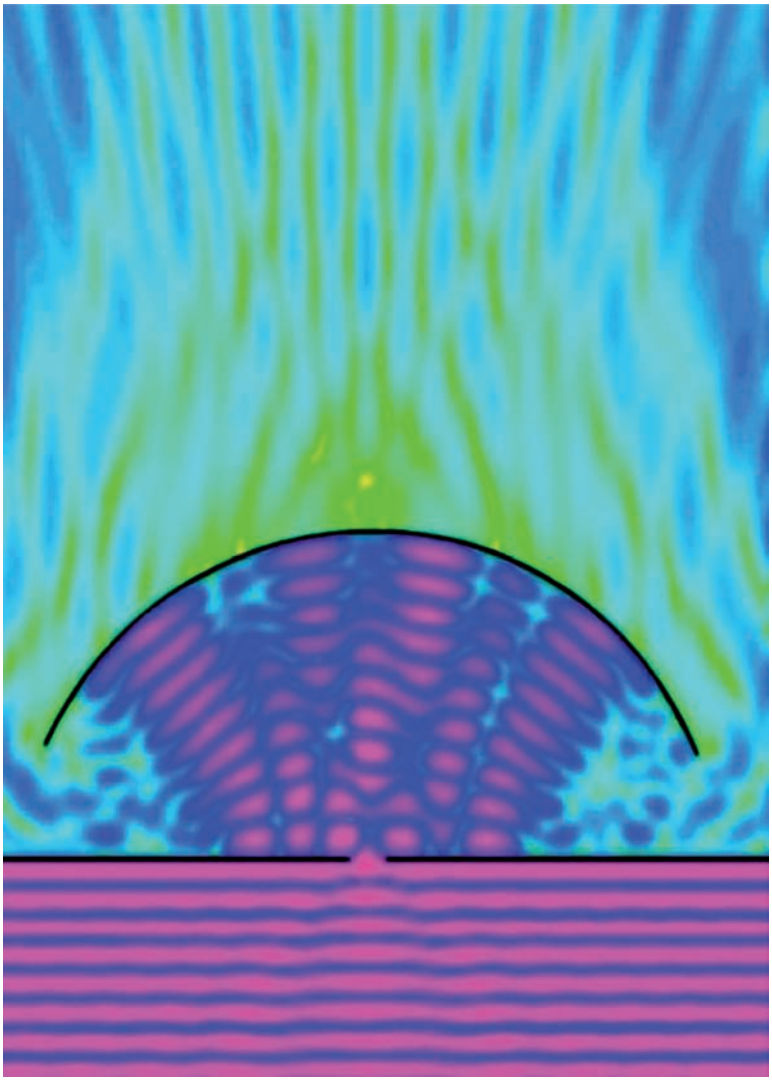

Figure 1.10. Heller's digital visualization (`https://ejheller.jalbum.net`) of the Westervelt resonator (of size $\sim 1\,\mu\text{m} = 10^{-6}$ m) built at Harvard in 1995 – see [**K*97**]. A quantum wave builds up in a resonant cavity between the straight and curved walls: the waves arrive from below and most of the wave energy is reflected back. However, a surprisingly large fraction of the energy finds its way through the tiny opening if the energy of the electron corresponds to the resonant energy (real part of the scattering resonance) of the cavity: to quote `https://ejheller.jalbum.net`, "usually it is pretty quiet in the cavity." Except for the possibility of escape through the side openings and tiny hole, classical electrons would be trapped in the cavity – the quantum waves leak out the sides. The Westervelt resonator is a quantum version of the Helmholtz resonator – see [**Zw17**, Figure 15] – where similar phenomena occur for acoustic waves.

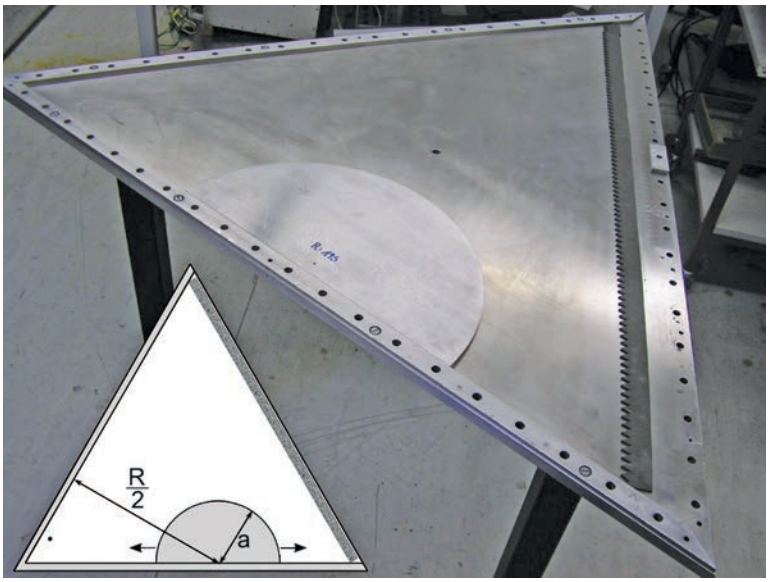

Figure 1.11. The experimental set-up used by the Stöckmann group in Marburg and the Kuhl group in Nice [**B*13**, **P*12**]. A three-disc symmetry reduced system is implemented in a microwave scattering experiment. The hard walls correspond to the Dirichlet boundary condition, that is, to odd solutions (by reflection) of the full problem. The absorbing barrier, which produces negligible reflection at the range of frequencies considered, models escape to infinity.

Figure 1.6 shows resonance peaks in a scanning tunneling microscope (STM) experiment conducted by Crommie et al. [**CLE93**]: the position of the peaks corresponds to the resonant states trapped by the corral. The trapping is much more pronounced in the experiment shown in Figure 1.9. It shows resonance peaks for an STM experiment where isospectral quantum corrals of CO molecules, instead of less densely packed iron atoms, are constructed – see [**M*08**] and references given there. The resonances are very close to eigenvalues of the Dirichlet Laplacian (rescaled by $\hbar^2/m_{\text{eff}}$ where m_{eff} is the effective mass of the Bloch electron). Mathematical results explaining existence of resonances created by a barrier (here formed by a corral of CO molecules) are presented in §7.3.

Figure 1.10 shows a visualization of the Westervelt resonator [**K*97**], a *nano*-version of the classical Helmholtz resonator (see [**DGM18**]). On the classical level, the cavity has a lot of trapping (see Figure 4.1 and §6.1) and classical electrons would get confined to the cavity for all times. The escape through the side openings and through the tiny opening at the bottom produces positive decay rates (non-zero imaginary parts of resonances).

The general mathematical mechanism of trapping producing long-lived resonances is described in §7.3.

Figure 1.11 shows an experimental set-up for microwave cavities used to study scattering resonances for chaotic systems. Density of resonances was investigated in this setting in [**P*12**] and is related to semiclassical upper bounds in §§3.4, 4.3, and 7.2. In [**B*13**] dependence of resonance-free strips on dynamical quantities was confirmed experimentally, and Chapter 6 contains related mathematical results and references.

Figure 1.12 shows a MEMS (acronym for *microelectromechanical systems*) resonator. The numerical calculations in that case are based on the complex scaling technique, presented in §4.5, adapted to finite element methods and known as the method of *perfectly matched layers* [**Be94**].

Figure 1.13 shows the profile of gravitational waves recently detected by the Laser Interferometer Gravitational-Wave Observatory (LIGO) and originating from a binary black hole merger. Resonances for such waves are known as *quasi-normal modes* in the physics literature and are the characteristic frequencies of the waves emitted during the ringdown phase of the merger, when the resulting single black hole settles down to its stationary state – see for instance [**KS99**], [**Dy12**], [**DZ13**] and §§5.7 and 6.3.

A survey [**Zw17**] presents recent mathematical results motivated by other physical phenomena such as quantum corrals [**BZH10**, **Ga19**, **GS15**], Helmholtz resonators [**DGM18**] (see also Figure 1.10), or dielectric cavities (see [**CW15**] for a physics survey and [**NS08**] for some theoretical results).

There are many topics which still await mathematical treatment, and one example is *long*-wavelength scattering (as opposed to semiclassical or *short*-wavelength scattering discussed in Part 3 of the book). For instance, for two closely placed scatterers, narrow *proximity* resonances (small imaginary parts) develop from broader resonances (large imaginary parts) of the individual scatterers – see Heller [**He96**]. Narrower resonances due to trapping introduced by two scatterers occur in the semiclassical regime (see §§6.6, and 7.3) but the mechanism described in [**He96**] is different.

1.4. OVERVIEW

To make the presentation more accessible we restrict ourselves to the simplest setting in which the theory is physically and mathematically relevant: compactly supported perturbations in odd dimensions. Many results, especially the ones based on complex scaling, are valid in all dimensions and for suitable non-compact perturbations, but for clarity of presentation we only provide pointers to the literature. The hope is that once the ideas are grasped in the technically less challenging setting, the references will become

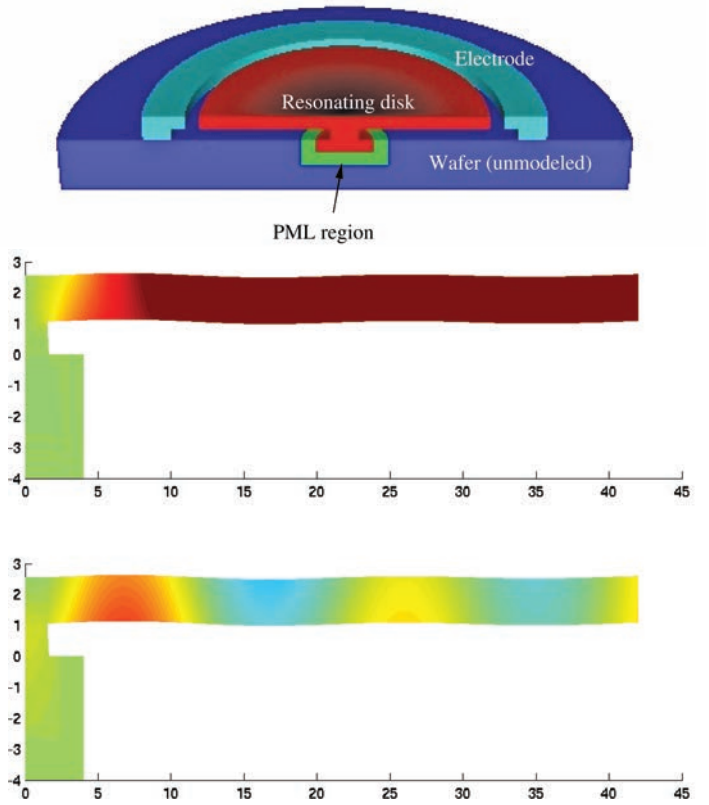

Figure 1.12. Top: a schematic representation of a MEMS device, a disc attached by a stem to an absorbing plate. Below: a computed resonant mode for this device; the top is colored by the amount of displacement in the radial direction, and the bottom is colored by the amount of displacement in the vertical direction. The computation was done using the complex scaling/PML (*perfectly matched layer*) methods of Bindel–Govindjee [**BG05**]. As explained there, for the resonance state shown in the figure, the coupling between the radial and vertical displacements gives this state a large imaginary part – in other words, a significant loss in oscillations.

accessible. In the case of scattering on asymptotically hyperbolic manifolds (Chapter 5) we present a general theory, as there are few advantages in restricting our attention to the hyperbolic space alone.

We now present brief descriptions of the content of the chapters.

Chapter 2: We cover basic theory of resonances in dimension one. Many fundamental concepts, such as outgoing solutions, meromorphic continuation of the resolvent, the relation of resonances to the scattering matrix,

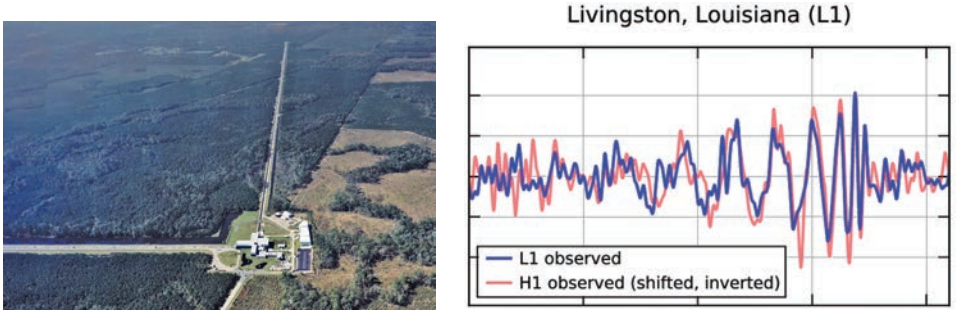

Figure 1.13. Left: an aerial view of the LIGO laboratory in Livingston, Louisiana, USA. Right: the gravitational wave signal observed on September 14, 2015 simultaneously by LIGO Livingstn (blue) and LIGO Hanford (red); see [**A*****16**] and [**V*14**]. The ringdown oscillations of the kind shown in Figure 1.1 and connected to quasi-normal modes (which is what scattering resonances are called in general relativity) have not been observed yet. What is shown here are oscillations due to a much stonger effect of a black hole merger.

trace formulas, and resonance expansions of waves, appear later in more complicated settings.

Chapter 3: Here the theory of scattering by compactly supported potentials in odd dimensions is presented in detail. This chapter can be used as an introduction to the study of more general settings (for instance, in the theory of zero resonances) and to the open problems in scattering by compactly supported potentials.

Chapter 4: This chapter is devoted to *black box* scattering, which allows a unified treatment of many different operators ranging from Laplacians on surfaces with constant curvature cusp ends to obstacle scattering in Euclidean space.

Chapter 5: One of the recent advances in geometric scattering is Vasy's approach to meromorphic continuation of resolvents for (even) asymptotically hyperbolic manifolds. The method was motivated by the study of scattering for black holes, and that connection is also explained.

Chapter 6: Resonance-free regions have been investigated in mathematical scattering theory since the seminal work of Lax–Phillips and Vaĭnberg (see §4.6). Semiclassical scattering with its connection to classical/quantum correspondence is the natural setting for investigating resonance-free regions.

Chapter 7: This last chapter is concerned with resonances generated by strong trapping phenomena such as the presence of barriers or singularities of $E \mapsto \int_{V(x)\geq E} dx$. We conclude with expansions of waves for strong trapping.

Appendices: We present notational conventions and references for basic techniques. Proofs of various results which are crucial for understanding the main text (such as Fredholm theory or propagation of singularities in the semiclassical setting) are presented in detail.

Acknowledgments for the figures:

- Figure 1.6 comes from [**CLE93**] and is reprinted with permission from the American Association for the Advancement of Science. The authors are grateful to Mike Crommie for allowing us to use this figure.
- Figure 1.9 comes from [**M*08**] and is reprinted with permission from the American Association for the Advancement of Science. The authors are grateful to Hari Manoharan for offering us this figure as an illustration of quantum resonances in a complex STM setting.
- Figure 1.10 comes from `https://ejheller.jalbum.net` and we are grateful to Eric Heller for permission to include it here.
- Figure 1.11 was provided to us by Ulrich Kuhl and represents an experimental set-up at his lab (`http://lpmc.unice.fr/Kuhl-Ulrich.html`). We are grateful to him and Hans-Jürgen Stöckmann for giving us access to their microwave experiments [**B*13**, **P*12**].
- Figure 1.12 is an original figure produced by David Bindel. The authors are grateful to him for providing the figure and the caption explaining the connection to [**BG05**]. We are also grateful to Sanjay Govindjee for discussions related to [**BG05**].
- Figure 1.13 comes from [**V*14**] and made use of figures obtained from the LIGO Open Science Center (`https://losc.ligo.org`), a service of LIGO Laboratory, the LIGO Scientific Collaboration, and the Virgo Collaboration. LIGO is funded by the U.S. National Science Foundation. Virgo is funded by the French Centre National de Recherche Scientifique (CNRS), the Italian Istituto Nazionale della Fisica Nucleare (INFN), and the Dutch Nikhef, with contributions from Polish and Hungarian institutes.

Dependence graph of sections